

2D Assembly of Confined Space toward Enhanced CO₂ Electroreduction

Peng Han, Zhijie Wang, Min Kuang, Yifei Wang, Jianing Liu, Linfeng Hu, Linping Qian, and Gengfeng Zheng*

Rational design of electrocatalysts toward efficient CO₂ electroreduction has the potential to reduce carbon emission and produce value-added chemicals. In this work, a strategy of constructing 2D confined-space as molecular reactors for enhanced electrocatalytic CO₂ reduction selectivity is demonstrated. Highly ordered 2D nanosheet lamella assemblies are achieved via weak molecular interaction of atomically thin titania nanosheets, a variety of cationic surfactants, and SnO₂ nanoparticles. The interlayer spacings can be tuned from 0.9 to 3.0 nm by using different surfactant molecules. These 2D assemblies of confined-space catalysts exhibit a strong size dependence of CO₂ electroreduction selectivity, with a peak Faradaic efficiency of 73% for formate production and excellent electrochemical stability at an optimal interspacing of ≈2.0 nm. This work suggests great potential for constructing new molecular-size reactors, for highly selective electrocatalytic CO₂ reduction.

1. Introduction

The fast and worldwide accumulation of carbon dioxide (CO₂) due to the fossil fuel utilization has been thriving active search of clean energy resources and solutions.^[1,2] In particular, the electrocatalytic reduction of CO₂ into value-added chemicals has the potential of offering an alternative fuel acquisition route that is capable of relieving the CO₂ production and accumulation.^[3–5] A major side reaction of the electrocatalytic CO₂ reduction (ECR) in aqueous electrolyte is known as hydrogen evolution reaction (HER), that is, the water reduction to produce H₂. Substantial research efforts have been invested to develop new electrocatalysts for enhancing the reactivity and selectivity of ECR, with the key foci on optimizing the composition,^[6,7] size,^[8,9] morphology,^[10,11] grain boundary,^[12]

crystal face,^[13,14] and oxidation states of electrocatalysts.^[15–17]


An alternative approach toward the ECR optimization is to design electrode architectures that can enable differential mass transfer profiles for CO₂ and water molecules.^[18] For instance, carbon-based, hydrophobic gas-diffusion-layers were reported to increase the transfer of CO₂ molecules toward catalyst surface.^[19] Inversed opal structures of Au,^[20] Ag,^[21] and Cu^[22] were prepared to inhibit the electrolyte diffusion and create an elevated local pH in the micrometer-sized pores, thus improving the ECR selectivity. Nonetheless, most electrocatalyst structures reported so far are based on diffusion channels with sizes from micrometers to

sub-100 nm scales. In spite of significant success during the past decades in the molecular assembly toward organic or inorganic mesostructures,^[23] to date, the construction of nanoscale building blocks into molecular-size confined spaces, such as from individual 2D nanostructures for enhanced ECR, has not been demonstrated.

As the molecular-induced assembly is mainly enabled by weak, noncovalent interactions (such as hydrophobic/hydrophilic effect^[24] and hydrogen bonds^[25]), the direct assembly of micrometer-scale 2D nanoscale building blocks into layer-by-layer (LbL) 3D architectures has remained substantially challenging and mainly relies on stronger driving forces such as electrostatic interactions.^[26,27] For instance, Sasaki and co-workers reported a static flocculation method to restack exfoliated Ti_{0.91}O₂ and Mg_{2/3}Al_{1/3}(OH)₂ nanosheets into layered sandwich structures, which presented a lamellar feature and multilayer spacings.^[28] Yamauchi and co-workers demonstrated the LbL assembly of graphene oxide held together by coordination polymers, followed by in situ crystallization to control the resulting lamellar structures.^[29] In these examples, as the nanosheet assemblies were held by strong electrostatic interactions, the interspacing distances between adjacent nanosheets were very close to the average thicknesses of individual nanosheets, thus not capable of serving molecular reactors. Recently, a pillared Ti₃C₂ MXene assembly using cetyltrimethylammonium bromide (CTAB) was reported to increase the interlayer thickness from 0.977 to 2.708 nm to facilitate for Li⁺ storage,^[30] while the lithiation reaction also took place in the bulk phase as well as for the tightly stacked layered sandwich structures.^[31,32]

P. Han, Z. Wang, M. Kuang, Y. Wang, J. Liu, Dr. L. Qian, Prof. G. Zheng
Laboratory of Advanced Materials
Department of Chemistry and Shanghai Key Laboratory of Molecular
Catalysis and Innovative Materials
Fudan University
Shanghai 200438, China
E-mail: gfzheng@fudan.edu.cn

Prof. L. Hu
Department of Materials Science
Fudan University
Shanghai 200438, China

 The ORCID identification number(s) for the author(s) of this article can be found under <https://doi.org/10.1002/aenm.201801230>.

DOI: 10.1002/aenm.201801230

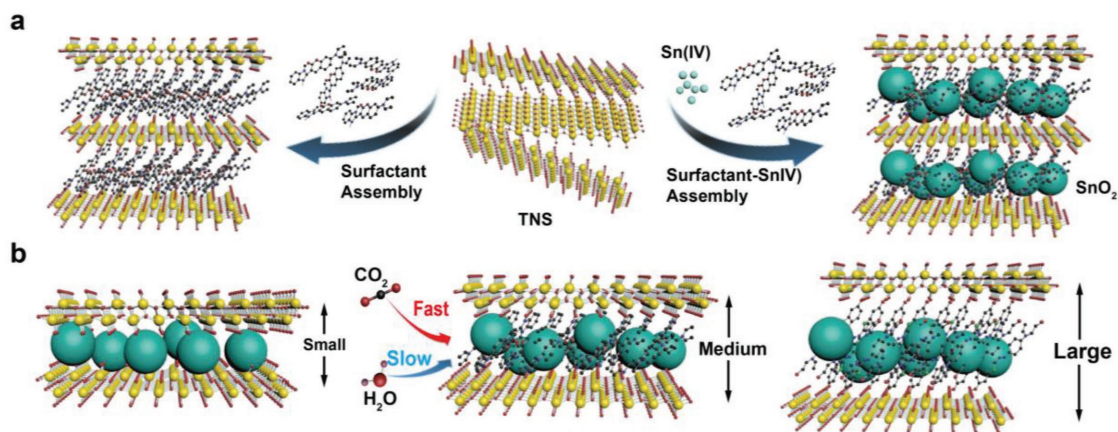


Figure 1. a) Schematic illustration of the surfactant-induced 2D assembly of confined space with TNS and SnO₂ nanoparticles. b) Schematic illustration of 2D TNS-SnO₂ assembly with different interlayer spacings for electrocatalytic CO₂ reduction.

Herein, we developed a strategy of constructing 2D confined-space assemblies as molecular-size electrocatalytic reactors for enhancing the ECR selectivity. These 2D confined space structures were assembled via weak molecular interaction between atomically thin titania nanosheets (TNSs) and a variety of cationic surfactants, where Sn(IV) ions could also be co-assembled into the interlayer spacing of neighboring nanosheets and further converted into SnO₂ nanoparticles by hydrolysis (Figure 1a). The interlayer spacing distances were well tailorable from ≈0.9 to 3.0 nm by the length of surfactant molecules and provided a hydrophobic environment and confined space, which allowed impeding the transfer of buffer electrolyte onto the SnO₂ electrocatalysts surface (Figure 1b) and thus tuning different selectivities of ECR and HER. At an optimal inter-spacing distance of ≈2.0 nm (Figure 1b, middle), an excellent Faradaic efficiency (FE) of CO₂ electroreduction to formate was achieved as ≈73%, significantly higher than that of the same SnO₂ electrocatalyst flocculated with TNS (Figure 1b, left) or embedded inside larger interlayer spacings of lamella assemblies (Figure 1b, right), suggesting a great potential of ECR selectivity enhancement by the confined space electrocatalytic systems.

2. Results and Discussion

The TNSs were fabricated by an osmotic swelling and exfoliation of lepidocrocite-type titanate (see Experimental Section in the Supporting Information).^[33] Atomic force microscopy image and height profile showed that the as-formed TNS had an average thickness of 1.0 ± 0.2 nm (Figure S1, Supporting Information), corresponding to the thickness of monolayer TiO₂ nanosheet (≈0.73 nm) with surface-adsorbed water molecules or cations.^[34] X-ray diffraction (XRD) patterns of TNS showed two weak reflections at 2θ of 48.3° and 62.6° (Figure S2a, Supporting Information), corresponding to the crystal structure of nanosheets inherited from protonic titanate and also indicating the low crystallinity of individual nanosheets.^[35] The direct mixing of TNS with cations such as NH₄⁺ or Na⁺ resulted in flocculation, which was also examined

by XRD. A set of new and distinctive peaks at 2θ of 9.4°, 17.9°, and 28.6° were observed (Figure S2b, Supporting Information), corresponding to the diffraction of (00*k*) planes ($k = 1, 2, 3, \dots$), similar to the previous reports of nanosheet flocculation via electrostatic interactions.^[36] The *d*-spacings of the (001) planes was calculated as ≈0.94 nm (designated as the TNS-0.9 sample), in good accord with the individual nanosheet thickness and indicating the direct stacking of nanosheets.

The assembly of individual nanosheets was then conducted by interaction with selected cationic surfactant molecules, including dodecyltrimethylammonium bromide (DTAB), tetradecyltrimethylammonium bromide (TTAB), CTAB, octadecyltrimethylammonium chloride (OTAC), 1H-benzimidazolium, 2-[7-(diethylamino)-2-oxo-2H-1-benzopyran-3-yl]-1,3-dimethyl-, methyl sulfate (XG), and benzothiazolium, 2-[2-[4-[ethyl(2-hydroxyethyl)amino]phenyl]diazanyl]-6-methoxy-3-methyl-, methyl sulfate (XR), respectively (see Figure S3 and Experimental Section in the Supporting Information). XRD patterns of the assembled structures revealed significant difference in the interlayer spacing values. As shown in Figure 2a and Figure S4 in the Supporting Information, each assembled sample presented a reflection series with (00*k*) planes ($k = 1, 2, 3, \dots$), indicating highly ordered lamella structures. For nanosheets coassembled with DTAB, TTAB, CTAB, or OTAC, the first order diffraction peaks corresponded to (001) interlayer spacings of 2.50, 2.59, 2.78, or 2.96 nm, respectively (Figure S4, Supporting Information). For nanosheets coassembled with XG or XR, the first-order diffraction peaks corresponded to interlayer spacings of 2.01 or 3.04 nm, respectively (Figure 2a). Although both XR and XG have similar molecular sizes, XR possesses more hydrophilic terminal groups than XG (Figure S3a,c, Supporting Information), which can lead to different assembly of these intercalated cationic surfactant molecules with TNS.^[37,38] As a result, the interlayer spacing of TNS-XR is different from that of TNS-XG.

High-resolution transmission electron microscopy (HRTEM) images of TNS assembled with XG or XR also showed a long-ordered stacking structure with 2.0 or 3.0 nm interlayer distance, respectively (Figure 2b and Figure S5, Supporting Information), in good accord with the XRD results. Compared

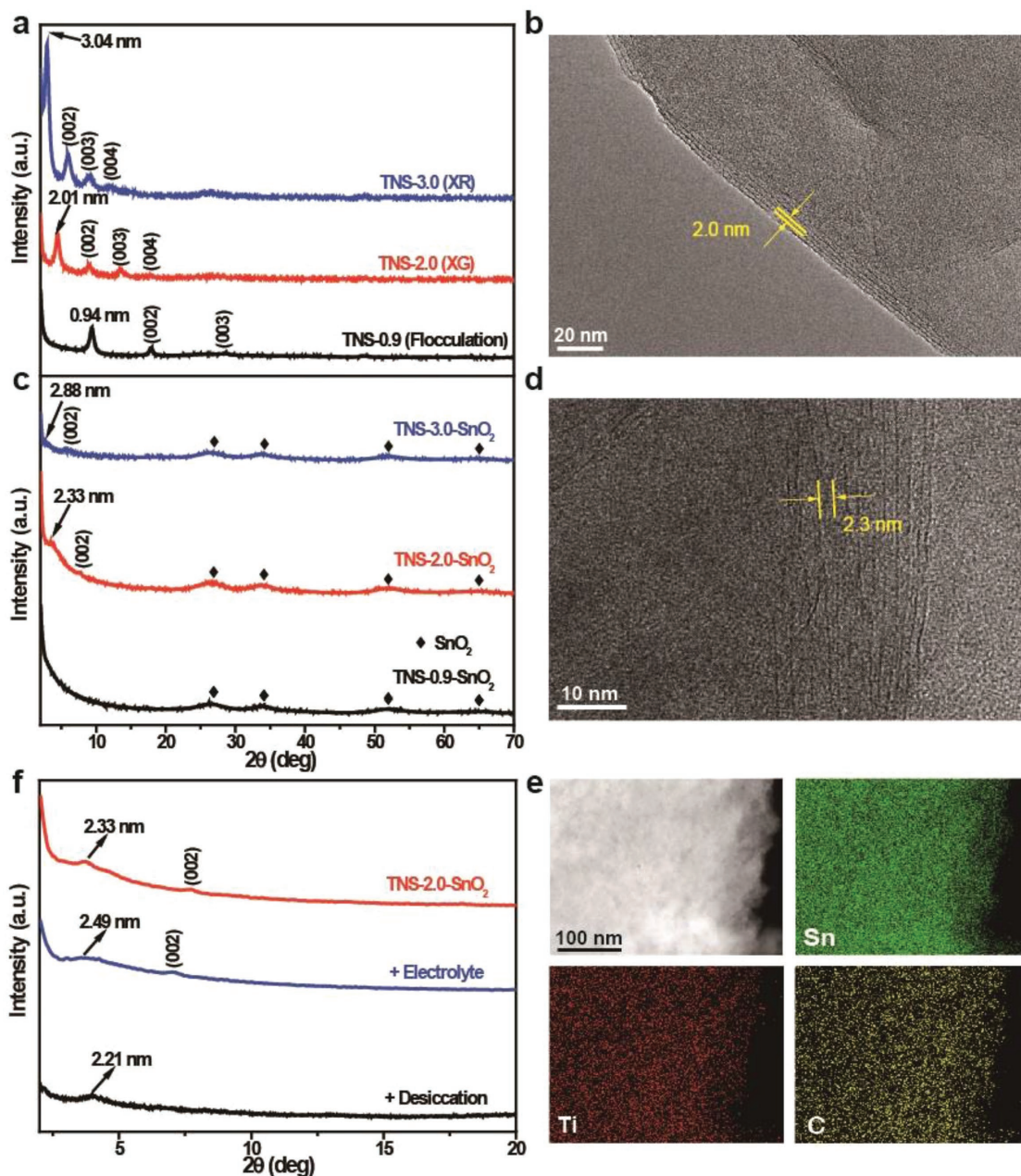


Figure 2. a) XRD patterns of TNS-0.9 (flocculation with NH_4^+ , black curve), TNS-2.0 (assembled with XG, red curve), and TNS-3.0 (assembled with XR, blue curve). (b) HRTEM of TNS-2.0. c) XRD patterns of TNS-0.9-SnO₂, TNS-2.0-SnO₂, and TNS-3.0-SnO₂. d) HRTEM of TNS-2.0-SnO₂. e) EDS elements mapping of TNS-2.0-SnO₂. The green, red, and yellow colors were denoted for Sn, Ti, and C, respectively. f) XRD patterns of TNS-2.0-SnO₂ (red curve), TNS-2.0-SnO₂ after immersing in 0.1 M KHCO₃ solution for 10 min (blue curve), and dried in vacuum after immersing in electrolyte (black curve).

to the individual nanosheet thickness of 0.94 nm, these increased and surfactant size-dependent interlayer spacings suggested that the TNSs were successfully assembled into highly ordered lamellar structures via the interaction with surfactant molecules.

The nanosheets were also coassembled with cationic surfactants and Sn(IV) ions into 2D assemblies, followed by hydrolysis of Sn(IV) into SnO₂ nanoparticles (see Experimental Section in the Supporting Information). XRD patterns of all the SnO₂-incorporated TNS assemblies present characteristic

diffraction peaks of 2θ between 20° and 70° (Figure 2c), which were well indexed to the rutile tetragonal phase SnO₂ (JCPDS card No. 46–1088). The average size of these SnO₂ nanoparticles was derived from the width of XRD diffraction peaks^[39] and calculated using the Scherrer equation as ≈ 1.8 nm. The order of the SnO₂-incorporated TNS assembly was also revealed by XRD. For the TNS flocculation with an original spacing of 0.94 nm, after the SnO₂ incorporation, the diffraction peaks below 20° disappeared (Figure 2c, black curve), which was accompanied by the emergence of disordered SnO₂ nanoparticles with

TNS (Figure S6, Supporting Information). For the TNS-XG assembly with an original spacing of 2.0 nm, as SnO₂ nanoparticles coassembled into interlayer spacing (designated as TNS-2.0-SnO₂), the XRD diffraction peaks shifted slightly to smaller angles and corresponded to an increased (001) interlayer spacing of 2.33 nm (Figure 2c, red curve). This increase of interlayer spacing was also confirmed by HRTEM images of the TNS-2.0-SnO₂ assembly, which also exhibited similar increase of interlayer spacings of 2.3 nm (Figure 2d). This increase of interlayer spacing was ascribed to the hydrolysis of Sn(IV) and the growth of SnO₂ nanoparticles between adjacent nanosheets, and was consistent with the calculated average size of SnO₂ nanoparticles (i.e., ≈1.8 nm). For TNS-3.0, the coassembly of XR and SnO₂ nanoparticles did not show an increase of the interlayer spacing (Figure 2c, blue curve), indicating that the original interlayer distance was large enough to accommodate the incorporation of SnO₂ nanoparticles. This hypothesis was consistent with the weight ratio of C/Ti determined by inductively coupled plasma atomic emission spectroscopy (Table S1, Supporting Information). For TNS-2.0 and TNS-2.0-SnO₂, the C/Ti ratios were similar, suggesting that the incorporation of additional SnO₂ increased the interlayer distance but did not decrease the amount of XG assembled inside layers. In contrast, the C/Ti ratio of TNS-3.0-SnO₂ was clearly lower than that of TNS-3.0, suggesting that the incorporation of SnO₂ did not expand the interlayer distance but decreased the amount of assembled XR.

The energy-dispersive spectroscopy (EDS) mapping images of the TNS-2.0-SnO₂ (Figure 2e) and TNS-3.0-SnO₂ (Figure S7, Supporting Information) samples indicated a uniform distribution of Ti, O, C, and Sn elements. The weight percentage of Sn incorporation was calculated to be ≈53% by inductively coupled plasma atomic emission spectroscopy (Table S1, Supporting Information). X-ray photoelectron spectroscopy (XPS) of the Sn 3d spectra further confirmed the oxidation state of Sn(IV) in the obtained assembly (Figure S8 and Table S2, Supporting Information). The peaks centered at 399.0 and 401.3 eV were attributed to the (CH₂)₃N and (CH₂)₃N⁺-R groups of the cationic surfactants, suggesting no covalent bonding existed between the TNS surface and surfactant molecules.

The capability of the 2D confined-space SnO₂ electrocatalyst for CO₂ reduction was first examined by the access of water molecules inside the nanosheet spacings. The TNS-2.0-SnO₂ assembly was incubated with 0.1 M KHCO₃ aqueous solution for 10 min, and then measured by XRD (Figure 2f, blue curve). The characteristic peaks further shifted to lower 2θ values, corresponding to an increase of interlayer spacing from 2.33 to 2.49 nm. Afterward, the desiccation of the TNS-2.0-SnO₂ assembly reduced of the interlayer spacing to 2.21 nm (Figure 2f, black curve).^[40] The TNS-3.0-SnO₂ sample also showed a similar trend for water molecule accessibility. The basal reflections of TNS-3.0-SnO₂ was shifted to a lower angle after immersing in 0.1 M KHCO₃ aqueous solution for 10 min, suggesting an increase of interlayer spacing from 2.88 to 3.02 nm (Figure S9a, Supporting Information). After desiccation, its interlayer spacing dropped to 2.79 nm. In contrast, the TNS-0.9-SnO₂ flocculation did not show any diffraction peaks below 20°, either with electrolyte or under desiccated conditions (Figure S9b, Supporting Information). These changes of the interlayer spacing indicated that water molecules can enter

and leave the confined spacings between adjacent nanosheets, which are a necessity for ECR.

The ECR capability of the SnO₂-incorporated nanosheet assemblies was then evaluated by linear sweep voltammetry measurement in a three-electrode system between -0.4 and -1.8 V versus reversible hydrogen electrode (RHE, see Experimental Section in the Supporting Information). All the potentials were converted and referred to RHE in this work. Compared to the pristine TNS assembly without SnO₂ (Figure 3a, black curve), the TNS-2.0-SnO₂ presented a reduced onset potential of -0.6 V but a similar current density (Figure 3a, red curve). The gas reduction products were examined by in-line gas chromatography (GC), and the liquid products were quantified by ¹H NMR spectroscopy. In all the voltages tested between -0.8 and -1.8 V, only three reduction products were obtained (Figure 3b), including formate (HCOOH or HCOO⁻) and carbon monoxide (CO) from ECR, and H₂ from HER. The FE values of all the reduction products were added to over ≈95%. With the increase of applied negative potential, the FE of formate production (FE_{HCOOH}) was significantly increased, which peaked at ≈73% at -1.6 V (Figure 3b). The FE values of H₂ and CO production were only about 19% and 3% at this potential, respectively. Further increase of the negative applied potential led to a decrease of FE_{HCOOH}, which may be attributed to the depletion of local CO₂ concentration around the electrode surface.^[11,41] Formate was previously reported as the major ECR product for the SnO₂-based electrocatalysts.^[3,39,42] In contrast, although the pristine TNS assembly without SnO₂ (i.e., TNS-2.0) showed a similar current density, the major reduction product was H₂ originated from water reduction (Figure 3c), due to the weak catalytic activity of titania for ECR. For example, at -1.6 V, the FE of H₂ production (FE_{H2}) was over 75%, while the combined FE values of formate and CO production were less than 20%.

The stability of the TNS-2.0-SnO₂ electrocatalyst was further demonstrated by continuous ECR measurement at -1.6 V for over 16 h (Figure 3d). Except for a quick drop at the beginning, the current density was stable at over 10 mA cm⁻² and the FE_{HCOOH} was well retained > 70% during the entire period, suggesting the excellent stability of the TNS-2.0-SnO₂ electrocatalyst. In addition, another control experiment of TNS-2.0-SnO₂ was carried out at -1.6 V in alternating between CO₂-saturated and Ar-saturated electrolytes, with ≈1 h for each electrolyte (Figure S10, Supporting Information). The current density reached to and was maintained at ≈8–10 mA cm⁻² in CO₂-saturated electrolyte, while it decreased to ≈2.5 mA cm⁻² in the durations of Ar-saturated electrolyte (mostly for HER). Thus, the ECR of the TNS-2.0-SnO₂ was confirmed to be attributed to the dissolved CO₂ in the solution, instead of the preadsorption of CO₂ in the interlayer spacings before electrochemical experiments.

The structural stabilities of each component of the assembled electrocatalysts were interrogated by XRD (Figure S11a, Supporting Information), XPS (Figure S11b, Supporting Information), HRTEM (Figure S11c, Supporting Information), and EDS elemental mapping (Figure S12, Supporting Information) after continuous electrochemical measurement. The TiO₂ nanosheets were well preserved. Although a portion of SnO₂ nanoparticles were electrochemically reduced to Sn, the

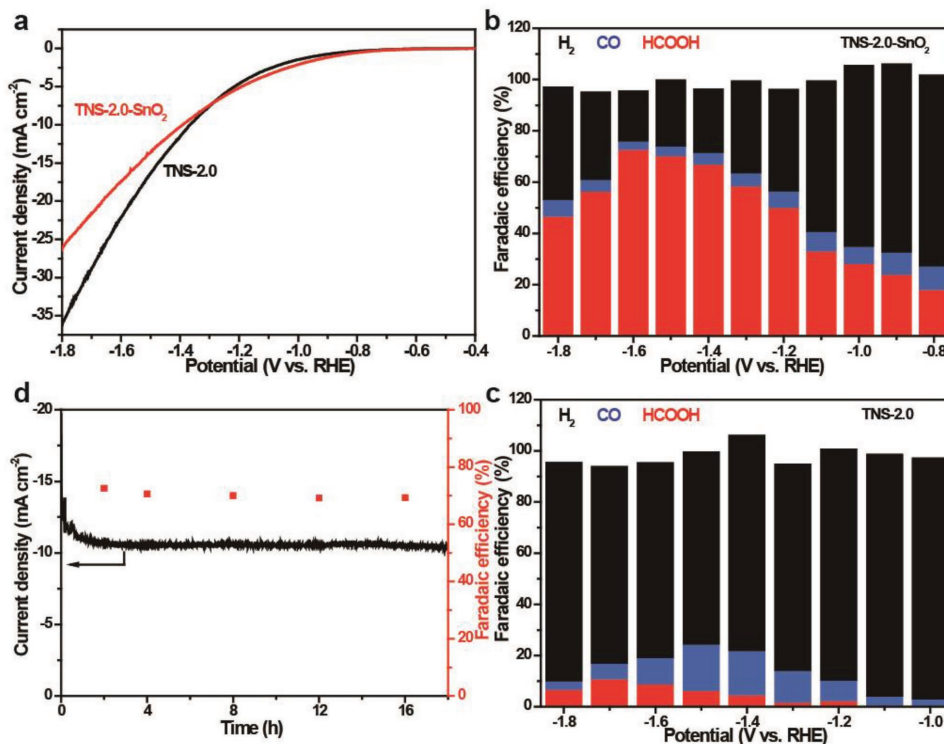


Figure 3. a) Linear sweep voltammetry of TNS-2.0 and TNS-2.0-SnO₂ in a CO₂-saturated 0.1 M KHCO₃ solution. The scan rate was 10 mV s⁻¹. b,c) Faradaic efficiencies of b) TNS-2.0-SnO₂ and c) TNS-2.0 at each applied potentials for 2 h. The three products were formate (red bars); CO (blue bars), and H₂ (black bars). d) Current versus time curve and Faradaic efficiency for HCOOH production of TNS-2.0-SnO₂ electrode in a CO₂-saturated 0.1 M KHCO₃ solution at an applied potential of -1.6 V versus RHE for >16 h.

resulted Sn/SnO_x electrocatalysts still functioned well in ECR, which was also reported by other groups.^[39,43] The structures of the 2D lamella assemblies were also well maintained, while the interlayer spacings slightly decreased from 2.33 to 2.02 nm (Figure S11a, Supporting Information), which were attributed to the partial reduction of SnO₂ to Sn nanoparticles as well as the partial loss of surfactant molecules inside layers. Nonetheless, the whole assembled structures still presented a robust ECR performance, as indicated by the electrochemical measurement data over the long time test (Figure 3d).

The ECR performances of nanosheet assemblies with different interlayer spacings were further interrogated. TNS-3.0-SnO₂ presented a smaller onset potential and higher current density than TNS-2.0-SnO₂ (Figure 4a), which clearly exceeded those of the direct assembly of TNS and SnO₂ flocculation (TNS-0.9-SnO₂). The comparison of FE values showed that TNS-2.0-SnO₂ presented the highest FE_{HCOOH} among these catalysts at the whole potential range tested, while TNS-0.9-SnO₂ had the lowest (Figure 4b). For instance, at -1.6 V, the FE_{HCOOH} values for TNS-2.0-SnO₂, TNS-3.0-SnO₂, and TNS-0.9-SnO₂ were 73%, 50%, and 39%, respectively.

To reveal the origin of this ECR selectivity difference, both the electrochemical active surface areas (ECSAs) and the volumetric CO₂ adsorption measurements of these catalysts were carried out. By measuring their electrochemical double-layer capacitances (C_{dl}), the ECSA values were calculated as 0.74, 1.53, and 0.55 mF cm⁻², for TNS-2.0-SnO₂, TNS-3.0-SnO₂, and TNS-0.9-SnO₂, respectively (Figure 4c and Figure S13,

Supporting Information). Compared to TNS-3.0-SnO₂, the relatively lower ECSA of TNS-2.0-SnO₂ suggested that its higher ECR selectivity was not mainly attributed to the ECSA. For the volumetric CO₂ adsorption measurement (Figure S14, Supporting Information), the TNS-2.0-SnO₂ presented a typical CO₂ adsorption isotherm of 2D materials^[15] and the highest adsorption capacities of 9.5 cm³ g⁻¹ at 1 atm, similar with TNS-3.0-SnO₂ (8.4 cm³ g⁻¹) but significantly higher than that of TNS-0.9-SnO₂ (3.6 cm³ g⁻¹).

The enhanced ECR selectivity of the TNS-2.0-SnO₂ sample was attributed to the reduced transfer of buffer electrolyte near the electrocatalyst surface. Previous studies have reported that the species that undergoes electrochemical reduction in CO₂ reduction in aqueous medium is dissolved CO₂,^[39,44] and the electrode mesostructuring can inhibit the mass transfer of protons and thus increase the local pH.^[20,21] A similar phenomenon also existed in our work. For TNS-3.0-SnO₂ with the largest interlayer spacing, the diffusion of water molecules was fast enough to equilibrate the local proton concentration, so the HER rate was still maintained. In contrast, for TNS-2.0-SnO₂, the interlayer spacing (≈2.0 nm) was not large enough so that the electrolyte transfer was impeded, which led to the decrease of HER. On the other hand, the proton transfer step has only limited effect on the ECR process,^[11,45,46] thus enhancing the FE of ECR over HER.

The aforementioned mechanism was confirmed by electrochemical measurement of TNS-2.0-SnO₂ in different bicarbonate electrolyte concentrations (from 0.1 to 1 M), as

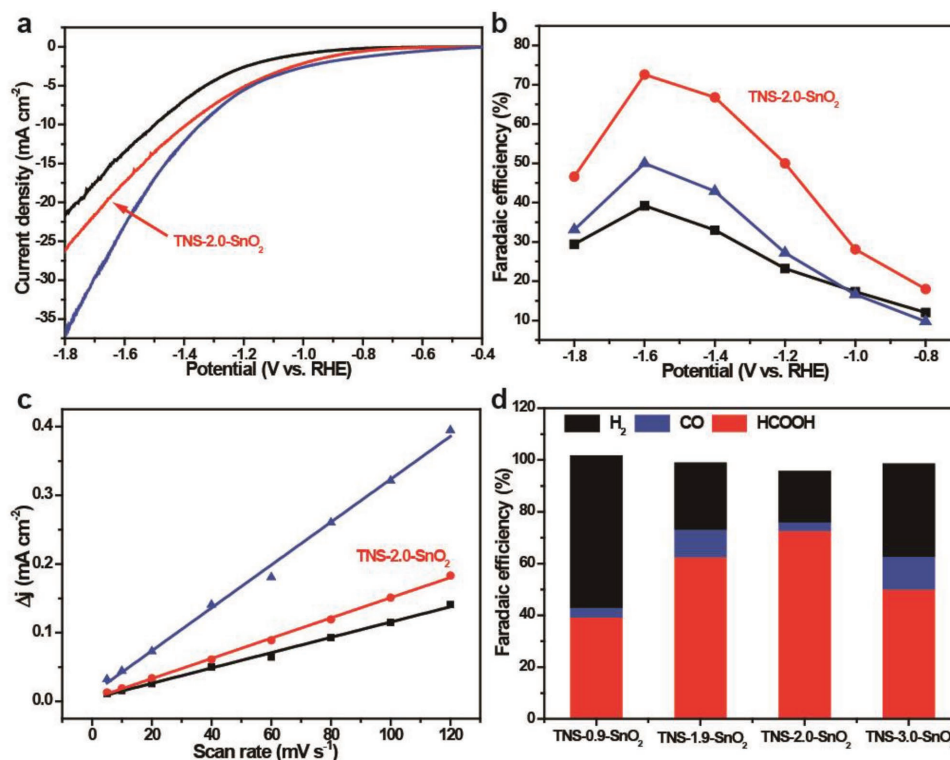


Figure 4. a) Linear sweep voltammetry of TNS-0.9-SnO₂, TNS-2.0-SnO₂, and TNS-3.0-SnO₂ in a CO₂-saturated 0.1 M KHCO₃ solution. The scan rate was 10 mV s⁻¹. b) Faradaic efficiencies for HCOOH production of TNS-0.9-SnO₂, TNS-2.0-SnO₂, and TNS-3.0-SnO₂ at each applied potentials for 2 h. c) Charging current density differences plotted against scan rates. The red, blue, and black curves were represented for TNS-2.0-SnO₂, TNS-3.0-SnO₂, and TNS-0.9-SnO₂, respectively. d) Faradaic efficiencies of TNS-0.9-SnO₂, TNS-1.9-SnO₂, TNS-2.0-SnO₂, and TNS-3.0-SnO₂. The three products were formate (red bars); CO (blue bars), and H₂ (black bars).

bicarbonate plays an important role as a proton donor and a buffer for ECR.^[39,44,47] As the increase of bicarbonate electrolyte strength can reduce the effect of the proton depletion near the electrode surface,^[20,21] a decrease of FE_{HCOOH}, and an increase of FE_{H₂} were observed (Figure S15a, Supporting Information). However, the partial current density of formate (j_{HCOOH}) of TNS-2.0-SnO₂ was essentially insensitive to the KHCO₃ concentration (Figure S15b, Supporting Information), consistent with the previous reports that the proton transfer step has limited influence on the whole ECR process.^[11,45,46]

The aforementioned observation was further supported by using another TNS-XR assembly, in which the surfactant (XR) concentration was tuned so that the spacing between adjacent nanosheets was ≈ 1.9 nm, confirmed by XRD pattern (Figure S16, Supporting Information). After the incorporation of SnO₂ using a similar approach aforementioned, the FE_{HCOOH} was 62% and the total FE_{HCOOH} and FE_{CO} reached 74% at -1.6 V (Figure 4d), which were comparable to TNS-2.0-SnO₂ with a similar layer spacing, but remarkably better than those of TNS-3.0-SnO₂ assembled from the same surfactant but different interlayer spacing (Figure S17, Supporting Information). Finally, the smallest interlayer spacing of TNS-0.9 flocculation did not achieve ordered assembly of SnO₂ nanoparticles inside 2D confined space, so the CO₂ reduction FE values of TNS-0.9 were the lowest, which were similar to the control TNS samples directly mixed with SnO₂ nanoparticles (designated as TNS-SnO₂, Figure S18, Supporting Information).

Taken together, all these results indicate that the ECR selectivity can be efficiently tuned by adjusting the interlayer spacing of the 2D nanosheet assemblies of confined space, which can be rationally configured by different surfactant molecule-induced interactions.

3. Conclusion

In summary, we have developed a 2D assembly of highly ordered lamella confined-space structures for efficient ECR catalysts. Several cationic surfactants and Sn(IV) ions were introduced to coassemble with TNS and adjust the interlayer spacing from ≈ 0.9 to 3.0 nm, thus achieving the incorporation of SnO₂ nanoparticles into tailorable interlayer spacing between adjacent TNS. The FE values for ECR were efficiently controlled by adjusting the confinement effect with interlayer spacing, among which TNS-2.0-SnO₂ with a medium spacing showed an excellent selectivity of 73%. Our work suggests attractive promises for assembling a host of new confined-space nanostructures with tailorable catalytic performance and selectivity toward highly efficient electrocatalytic CO₂ reduction.

Supporting Information

Supporting Information is available from the Wiley Online Library or from the author.

Acknowledgements

The authors thank the following funding agencies for supporting this work: the National Key Research and Development Program of China (2017YFA0206901, 2018YFA0209401), the Natural Science Foundation of China (21473038, 21773036), and the Key Basic Research Program of Science and Technology Commission of Shanghai Municipality (17JC1400100).

Conflict of Interest

The authors declare no conflict of interest.

Keywords

2D nanosheets, assembly, electrocatalytic CO₂ reduction, Faradaic efficiency, interlayer spacings

Received: April 24, 2018

Revised: June 14, 2018

Published online: July 5, 2018

- [1] Z. W. Seh, J. Kibsgaard, C. F. Dickens, I. B. Chorkendorff, J. K. Nørskov, T. F. Jaramillo, *Science* **2017**, *355*, 146.
- [2] J. H. Wu, Y. Huang, W. Ye, Y. G. Li, *Adv. Sci.* **2017**, *4*, 1700194.
- [3] D. D. Zhu, J. L. Liu, S. Z. Qiao, *Adv. Mater.* **2016**, *28*, 3423.
- [4] L. Zhang, Z. J. Zhao, J. L. Gong, *Angew. Chem., Int. Ed.* **2017**, *56*, 11326.
- [5] A. Vasileff, Y. Zheng, S. Z. Qiao, *Adv. Energy Mater.* **2017**, *7*, 1700759.
- [6] Z. Y. Chang, S. J. Huo, W. Zhang, J. H. Fang, H. L. Wang, *J. Phys. Chem. C* **2017**, *121*, 11368.
- [7] Z. Weng, X. Zhang, Y. S. Wu, S. J. Huo, J. B. Jiang, W. Liu, G. J. He, Y. Y. Liang, H. L. Wang, *Angew. Chem., Int. Ed.* **2017**, *56*, 13135.
- [8] R. Reske, H. Mistry, F. Behafarid, B. R. Cuenya, P. Strasser, *J. Am. Chem. Soc.* **2014**, *136*, 6978.
- [9] D. F. Gao, H. Zhou, J. Wang, S. Miao, F. Yang, G. X. Wang, J. G. Wang, X. H. Bao, *J. Am. Chem. Soc.* **2015**, *137*, 4288.
- [10] Y. F. Li, F. Cui, M. B. Ross, D. Kim, Y. Sun, P. D. Yang, *Nano Lett.* **2017**, *17*, 1312.
- [11] F. W. Li, L. Chen, G. P. Knowles, D. R. MacFarlane, J. Zhang, *Angew. Chem., Int. Ed.* **2017**, *56*, 505.
- [12] K. Jiang, H. Wang, W. B. Cai, H. T. Wang, *ACS Nano* **2017**, *11*, 6451.
- [13] J. H. Koh, D. H. Won, T. Eom, N. K. Kim, K. D. Jung, H. Kim, Y. J. Hwang, B. K. Min, *ACS Catal.* **2017**, *7*, 5071.
- [14] K. Jiang, R. B. Sandberg, A. J. Akey, X. Liu, D. C. Bell, J. K. Nørskov, K. Chan, H. Wang, *Nat. Catal.* **2018**, *1*, 111.
- [15] S. Gao, Y. Lin, X. C. Jiao, Y. F. Sun, Q. Q. Luo, W. H. Zhang, D. Q. Li, J. L. Yang, Y. Xie, *Nature* **2016**, *529*, 68.
- [16] Y. F. Sun, F. C. Lei, S. Gao, B. C. Pan, J. F. Zhou, Y. Xie, *Angew. Chem., Int. Ed.* **2013**, *52*, 10569.
- [17] K. Jiang, P. Kharel, Y. D. Peng, M. K. Gangishetty, H. Y. G. Lin, E. Stavitski, K. Attenkofer, H. T. Wang, *ACS Sustain. Chem. Eng.* **2017**, *5*, 8529.
- [18] S. Zhang, P. Kang, S. Ubnoske, M. K. Brennaman, N. Song, R. L. House, J. T. Glass, T. J. Meyer, *J. Am. Chem. Soc.* **2014**, *136*, 7845.
- [19] T. Abe, T. Yoshida, S. Tokita, F. Taguchi, H. Imai, M. Kaneko, *J. Electroanal. Chem.* **1996**, *412*, 125.
- [20] A. S. Hall, Y. Yoon, A. Wuttig, Y. Surendranath, *J. Am. Chem. Soc.* **2015**, *137*, 14834.
- [21] Y. Yoon, A. S. Hall, Y. Surendranath, *Angew. Chem., Int. Ed.* **2016**, *55*, 15282.
- [22] K. D. Yang, W. R. Ko, J. H. Lee, S. J. Kim, H. Lee, M. H. Lee, K. T. Nam, *Angew. Chem., Int. Ed.* **2017**, *56*, 796.
- [23] W. Li, J. Liu, D. Y. Zhao, *Nat. Rev. Mater.* **2016**, *1*, 16023.
- [24] Z. Q. Sun, T. Liao, Y. H. Dou, S. M. Hwang, M. S. Park, L. Jiang, J. H. Kim, S. X. Dou, *Nat. Commun.* **2014**, *5*, 3813.
- [25] B. Kong, J. Tang, Y. Y. Zhang, T. Jiang, X. G. Gong, C. X. Peng, J. Wei, J. P. Yang, Y. C. Wang, X. B. Wang, G. F. Zheng, C. Selomulya, D. Y. Zhao, *Nat. Chem.* **2016**, *8*, 171.
- [26] M. Wang, X. D. Duan, Y. X. Xu, X. F. Duan, *ACS Nano* **2016**, *10*, 7231.
- [27] J. F. Ping, Y. X. Wang, Q. P. Lu, B. Chen, J. Z. Chen, Y. Huang, Q. L. Ma, C. L. Tan, J. Yang, X. H. Cao, Z. J. Wang, J. Wu, Y. B. Ying, H. Zhang, *Adv. Mater.* **2016**, *28*, 7640.
- [28] L. Li, R. Z. Ma, Y. Ebina, K. Fukuda, K. Takada, T. Sasaki, *J. Am. Chem. Soc.* **2007**, *129*, 8000.
- [29] M. B. Zakaria, C. L. Li, Q. M. Ji, B. Jiang, S. Tominaka, Y. Ide, J. P. Hill, K. Ariga, Y. Yamauchi, *Angew. Chem., Int. Ed.* **2016**, *55*, 8426.
- [30] J. M. Luo, W. K. Zhang, H. D. Yuan, C. B. Jin, L. Y. Zhang, H. Huang, C. Liang, Y. Xia, J. Zhang, Y. P. Gan, X. Y. Tao, *ACS Nano* **2017**, *11*, 2459.
- [31] Y. F. Sun, J. B. Zhu, L. F. Bai, Q. Y. Li, X. Zhang, W. Tong, Y. Xie, *Inorg. Chem. Front.* **2014**, *1*, 58.
- [32] X. Cao, C. Tan, X. Zhang, W. Zhao, H. Zhang, *Adv. Mater.* **2016**, *28*, 6167.
- [33] T. Sasaki, M. Watanabe, *J. Am. Chem. Soc.* **1998**, *120*, 4682.
- [34] T. Sasaki, Y. Ebina, Y. Kitami, M. Watanabe, T. Oikawa, *J. Phys. Chem. B* **2001**, *105*, 6116.
- [35] H. Xin, R. Z. Ma, L. Z. Wang, Y. S. Ebina, K. Takada, T. Sasaki, *Appl. Phys. Lett.* **2004**, *85*, 4187.
- [36] T. Sasaki, M. Watanabe, H. Hashizume, H. Yamada, H. Nakazawa, *J. Am. Chem. Soc.* **1996**, *118*, 832.
- [37] C. Yu, J. Fan, B. Tian, G. D. Stucky, D. Zhao, *J. Phys. Chem. B* **2003**, *107*, 13368.
- [38] Y. Wan, D. Zhao, *Chem. Rev.* **2007**, *107*, 2821.
- [39] S. Zhang, P. Kang, T. J. Meyer, *J. Am. Chem. Soc.* **2014**, *136*, 1734.
- [40] T. Sasaki, Y. Ebina, T. Tanaka, M. Harada, M. Watanabe, G. Decher, *Chem. Mater.* **2001**, *13*, 4661.
- [41] N. Han, Y. Wang, L. Ma, J. Wen, J. Li, H. Zheng, K. Nie, X. Wang, F. Zhao, Y. Li, *Chem* **2017**, *3*, 652.
- [42] Y. Hori, H. Wakebe, T. Tsukamoto, O. Koga, *Electrochim. Acta* **1994**, *39*, 1833.
- [43] M. F. Baruch, J. E. Pander, J. L. White, A. B. Bocarsly, *ACS Catal.* **2015**, *5*, 3148.
- [44] M. Dunwell, Q. Lu, J. M. Heyes, J. Rosen, J. G. Chen, Y. Yan, F. Jiao, B. Xu, *J. Am. Chem. Soc.* **2017**, *139*, 3774.
- [45] A. Wuttig, M. Yaguchi, K. Motobayashi, Y. Surendranath, *Proc. Natl. Acad. Sci. USA* **2016**, *113*, 4585.
- [46] A. Wuttig, Y. Yoon, J. Ryu, Y. Surendranath, *J. Am. Chem. Soc.* **2017**, *139*, 17109.
- [47] S. Q. Zhu, B. Jiang, W. B. Cai, M. H. Shao, *J. Am. Chem. Soc.* **2017**, *139*, 15664.